# Influence of Geometry on Quasi-Ballistic Behavior in Silicon Nanowire Geometric Diodes

Kelly L. White<sup>†</sup>, Max A. Umantsev<sup>†</sup>, Jeremy D. Low, James P. Custer Jr., and James F. Cahoon\*

\* corresponding author: <u>ifcahoon@unc.edu</u>

† K.W. and M.U. contributed equally to this paper.

Department of Chemistry, University of North Carolina at Chapel Hill, Chapel Hill, NC 27599-3290, USA.

**Keywords**. nanowire, geometric diode, electron ratchet, Monte Carlo simulation, ballistic transport

#### **ABSTRACT**

Diodes are a basic component of electrical circuits to control the flow of charge, and geometric diodes (GDs) are a special class that can operate using ballistic or quasi-ballistic transport in conjunction with geometric asymmetry to direct charge carriers preferentially in one direction, enabling an electron ratcheting effect. Nanomaterials present a unique platform for development of GDs, and silicon nanowire (NW) based GDs—cylindrically symmetric but translationally asymmetric three-dimensional nanostructures—have recently been demonstrated functioning at room temperature. These devices can theoretically achieve near zero-bias turn-on voltage and rectify up to THz frequencies. Here, we synthesize silicon NW GDs and fabricate single-NW devices from which significant changes in diode performance are observed from relatively minor changes in geometry. To elucidate the interplay between geometry and ballistic behavior, we develop a Monte Carlo simulation that describes the quasi-ballistic behavior of

electrons within a three-dimensional NW GD. We examine the effects of doping level, temperature, and geometry on charge carrier transport, revealing the relationships between charge carrier mean free path (MFP), specular reflection at surfaces, and geometry on GD performance. As expected, geometry strongly influences performance by directing or blocking charge carrier passage through the nanostructure. Interestingly, we find that the blocking effect is at least as important as the directing effect. Moreover, within certain geometric limits, the diode behavior is less sensitive to MFP than might be initially expected because of the short relevant length scales and importance of the blocking effect. The results provide guidelines for the future design of NW GDs and enable the prediction and interpretation of trends in experimental results. Improved understanding of quasi-ballistic transport is crucial to guiding future experiments toward realizing THz rectification for applications in high-speed data transfer and long-wavelength energy harvesting.

### **INTRODUCTION**

A ratcheting mechanism can describe a broad set of physical phenomena in inherently asymmetric systems, <sup>1-4</sup> including the unidirectional motion of motor molecules and proteins, <sup>5, 6</sup> particle separation in microfluidic devices, <sup>7, 8</sup> and the directed flow of current in electron ratchets. <sup>1</sup> Electron ratchets, geometric diodes (GDs), and ballistic rectifiers, are related concepts that have been of continuing interest to condensed matter physics, chemistry, and electrical engineering disciplines since the concept was introduced more than 70 years ago. <sup>9</sup> In general, an electron ratchet is a system with spatial inversion asymmetry (*i.e.* broken spatial inversion symmetry) that is out of thermal equilibrium and subjected to a time-varying force (*e.g.* alternating current (AC) signals) with a time average of zero. The combination of inversion

asymmetry and disequilibrium allows the system to rectify a time-varying force to produce a net direct current (DC) and electrical power. At thermal equilibrium, thermal fluctuations cancel out, and electron ratchet systems produce no time-averaged DC power (as required by the Second Law of Thermodynamics).

There are several ways in which electron ratchets can be classified. Most fundamentally, they can be classified as either tilting or flashing ratchets. A tilting ratchet contains a constant, asymmetric potential (or shape) with a time-varying bias whereas a flashing ratchet contains a time-varying asymmetric potential and a constant bias (typically zero). In addition, electron ratchets can be classified as those that rely on ballistic or quasi-ballistic transport of charge carriers and those that do not (non-ballistic, or diffusive, electron ratchets), where the differences between ballistic, quasi-ballistic, and diffusion transport are illustrated in Figure 1A. The term quasi-ballistic refers to geometric, temperature (*T*), or doping conditions where some degree of charge carrier scattering is expected within the nominally ballistic region, but the degree and effect of scattering is sufficiently small that a ballistic mechanism still results in a GD effect.

Ballistic electron ratchet systems (also called ballistic rectifiers), rely on the ballistic motion of charge carriers in an asymmetric geometry and are best classified as tilting ratchets. They have been reported in two-dimensional (2D) systems with relatively long mean free paths (MFPs) such as 2D electron gases<sup>4, 10-21</sup> (typically GaAs/AlGaAs quantum wells) and the 2D material graphene.<sup>22-28</sup> Ballistic rectifiers are often fabricated with asymmetric "quantum dots" (*e.g.* triangle or semicircle shapes) within the 2D electron gases or materials, and they can be configured as two or four-terminal devices. Under a DC bias, these systems can exhibit non-linear (voltage sign and magnitude dependent) conductance originating from a GD effect in which ballistic charge carriers have differing probabilities of transmission between electrical

contacts depending upon their initial position, momentum, and the system geometry. Upon the application of AC signals, these systems can rectify to produce a DC current/voltage as a result of the ratcheting mechanism induced by the asymmetric morphology and transport. These GD electron ratchet systems are termed ballistic (or quasi-ballistic) because the effect is induced by specular (or quasi-specular) reflection at the asymmetric system boundaries of charge carriers that follow otherwise linear (or curvilinear) ballistic trajectories, resulting in the higher transmission of charge carriers in one direction over the other.

To achieve ballistic or quasi-ballistic transport, the length scales of the geometry must be similar to the MFP of the charge carriers. This type of charge transport has been characterized in the Landauer-Büttiker formalism, <sup>29-33</sup> which was developed to describe charge flow through a 1D ballistic point contact where classical descriptions cannot explain experimental behavior. Originally it was designed for two reservoirs of charges connected by a 1D channel, <sup>30</sup> but was later generalized to include more than one channel. <sup>31, 33</sup>

As illustrated in Figure 1B, Si nanowire (NW) GDs are translationally-asymmetric but cylindrically-symmetric nanostructures that function as electron ratchets at room *T* by preferentially directing quasi-ballistic electron transport through specular reflection at the NW surface. They have recently been shown to rectify at frequencies through at least 40 GHz, and their performance can depend sensitively on various geometric parameters, as illustrated in Figure 1C.<sup>34</sup> In this work, we demonstrate the fabrication of exemplary Si NW GD devices and analyze the significant relationship between geometry and diode performance by developing a Monte Carlo simulation of quasi-ballistic transport in NW GDs. Understanding the quasi-ballistic nature of the charge carriers in GDs is critical to explaining their behavior and fully realizing their advantages, such as near zero-bias turn-on voltage and exceptionally high

frequency response into the THz regime.<sup>23, 34</sup> These advantages can unlock many potential applications such as high-speed data transfer, astronomical exploration, materials defect characterization, security screening, and long wavelength energy harvesting.<sup>35</sup>

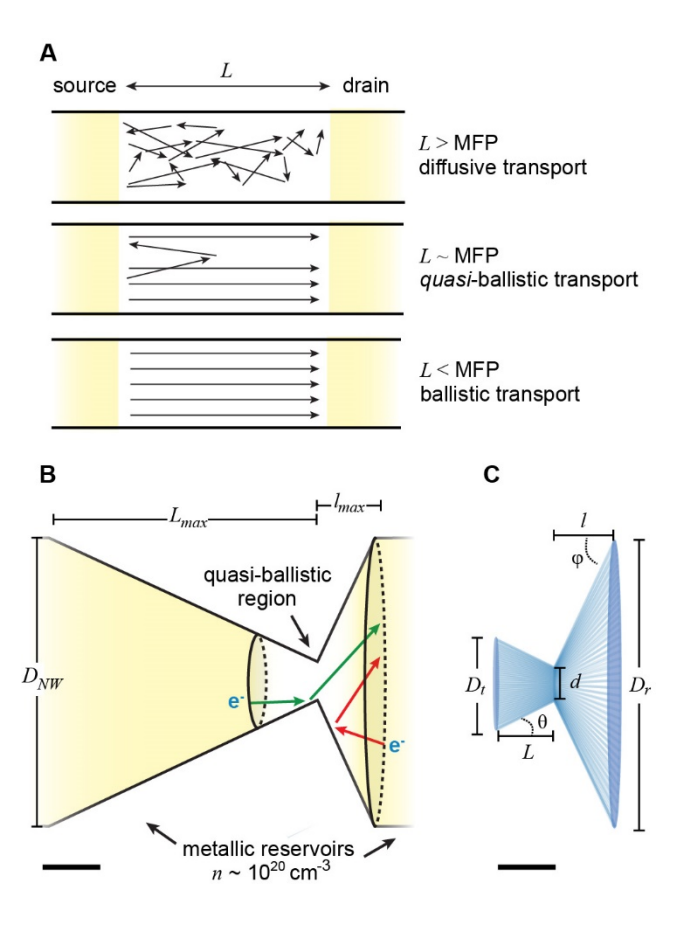


Figure 1. Ballistic effects in NW GDs. (A) Illustration of particle trajectories during diffusive, quasi-ballistic, and ballistic charge transport. (B) Schematic of a NW GD with a sawtooth geometry and degenerately doped n-type sections (yellow) that serve as metallic reservoirs and a quasi-ballistic section (white) into which electrons are injected and specularly reflect off the transmission taper (left) and rejection taper (right). Included geometric parameters are wire diameter ( $D_{NW}$ ), maximum transmission taper length ( $L_{max}$ ), and maximum rejection taper length ( $l_{max}$ ); scale bar, 20 nm. (C) Schematic of a NW GD quasi-ballistic region with geometric

parameters including transmission taper diameter  $(D_l)$ , rejection taper diameter  $(D_r)$ , constriction diameter (d), transmission taper length (L), rejection taper length (l), transmission taper angle  $(\theta)$ , and rejection taper angle  $(\varphi)$ ; scale bar, 20 nm.

#### RESULTS AND DISCUSSION

$$\delta = -\frac{I^{+}(+|V_{app}|)}{I^{-}(-|V_{app}|)}.$$
 (1)

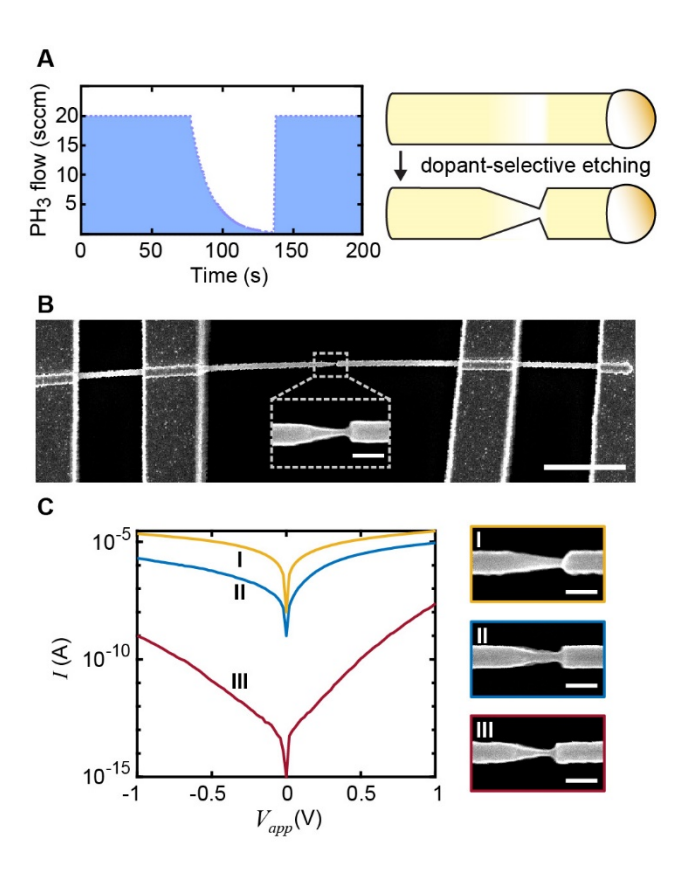


Figure 2. Synthesis, fabrication, and measurement of Si NW GDs. (A) Schematic of NW GD fabrication through dopant-encoded VLS growth with the PH<sub>3</sub> dopant precursor gas flow profile (left) that encodes a dopant density gradient in the NW for subsequent dopant-selective wet chemical etching to create the GD sawtooth geometry (right). (B) SEM image of single NW device; scale bar, 2 μm. Inset: higher magnification SEM image of the GD portion of the NW; scale bar, 200 nm. (C) Semi-logarithmic *I-V* curves (left) and SEM images (right) from three Si NW GD devices; scale bars, 200 nm.

Figure 2C displays I-V curves and SEM images measured from three Si NW GD devices, and the  $\delta$  values calculated from data from devices labeled I, II, and III are 1.5, 6, and 23, respectively, for  $|V_{app}| = 1$  V. The primary differences between these structures are geometric, including the rejection taper angle  $\varphi$  and the constriction diameter d. For instance, device I has a

smaller  $\varphi$  and device III has a smaller d than the other devices. These experimental results illustrate that minor changes in geometry can have significant impact on GD performance.

To more fully understand the influence of geometry on Si NW GD behavior, we developed a MC model for simulating the ballistic nature of charge carriers within NW GDs taking motivation from the Landauer-Büttiker formalism and its generalizations.<sup>37</sup> Considering the encoded dopant profile of the experimentally demonstrated Si NW GDs, the full 3D Monte Carlo (MC) simulation developed herein treats the NW GD as two metallic reservoirs (corresponding to degenerately-doped n-type regions) connected by a quasi-ballistic region into which electrons are injected and specularly reflect (Figure 1B). This quasi-ballistic region has an asymmetric 'sawtooth' geometry that is the hallmark of a two-terminal NW GD. As shown in Figure 1C, it is composed of two conical sections denoted the transmission taper (defined by angle  $\theta$  and length L) and rejection taper (defined by angle  $\varphi$  and length L) connected by a constriction of diameter d.

The MC method is a standard method for simulating carrier transport in semiconductors<sup>38</sup> and is appropriate for investigating the behavior of ballistic carrier transport in NW GDs by modeling the trajectories of single charge carriers within the nanostructure subject to bulk and surface scattering events. As detailed in the Methods section and Supporting Information, our MC model follows a standard model for Si and an algorithm outlined by Lundstrom.<sup>39</sup>

To determine the MFP of charge carriers, we considered a free carrier in the bulk under no field and without physical boundaries. For a given T and  $N_D$ , the MFP was taken as the average length of all free paths between scattering events within the MC simulation. Figure 3A displays a heat map of MFP for carriers traveling through bulk Si with varying  $N_D$  and T, allowing a specific MFP to be identified for a given set of parameters.

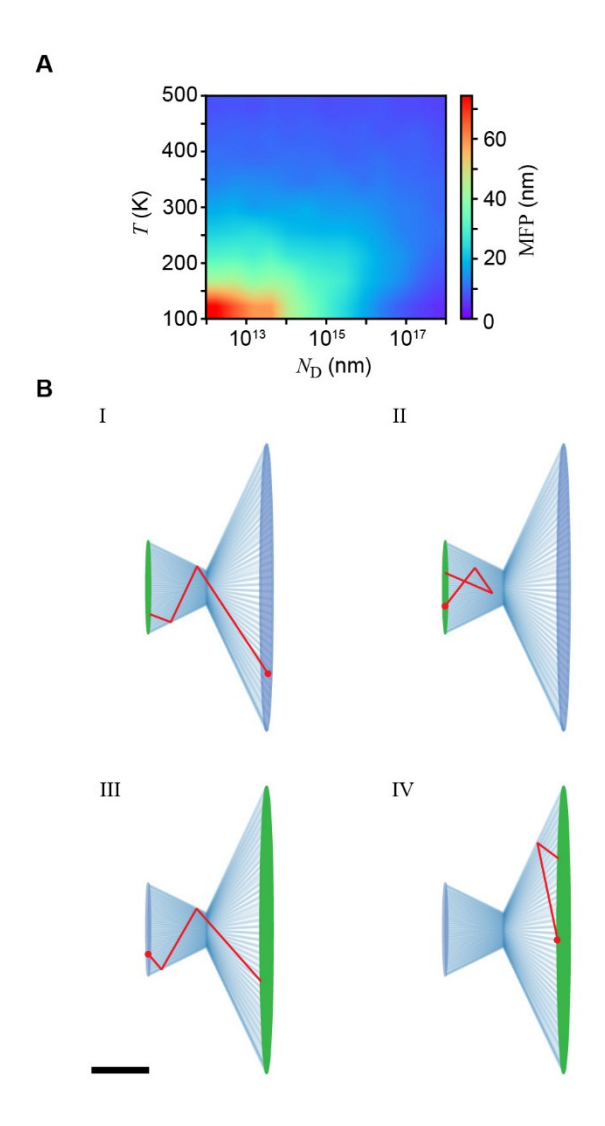


**Figure 3. MC simulation methods.** (**A**) Heat map of MFP for carriers traveling through bulk Si with varying  $N_D$  and T. (**B**) Schematic illustrations of particles injected from the transmission side at terminal t (I, II) and rejection side at terminal r (III, IV) of the structure and passing either successfully (I, III) or unsuccessfully (II, IV) from one side to the other through the constriction; scale bar, 20 nm.

To simulate a NW GD device, we introduce radial boundaries representative of the asymmetric NW geometry, and as illustrated in Figure 3B, we represent the axial termination of the GD device as co-parallel planes at either end (termed terminal *t* and terminal *r* for the terminals on the transmission side and rejection side, respectively) that define the quasi-ballistic region of the device. These planes act to define both the start points (located on green discs in Figure 3B) and end points (located at red circles in Figure 3B) of each MC simulation trajectory within the physical bounds of the structure. Simulations are informed by the elastic resistor model that considers electrons traveling along fixed energy channels between two contacts driven by the difference in electrochemical potential between the contacts and not by an electric field.<sup>45</sup> Thus, except where explicitly noted, we consider quasi-ballistic transport within the quasi-ballistic region without the presence of an electric field.

Motivated by the Landauer-Büttiker formalism,<sup>31, 32</sup> which can be modified to account for nonlinear transport,<sup>11</sup> we model the DC asymmetry in terms of charge carrier transmission between the end terminals of the quasi-ballistic simulation domain. As discussed previously,<sup>34</sup> the theoretical  $\delta$  of a NW GD, under the assumptions that  $V_{app}$  introduces nonlinearity by altering the momentum distribution of charge carriers<sup>11</sup> and that transmission probabilities against the applied field are zero, can be approximated as the ratio:

$$\delta \approx \frac{T_t^+}{T_r^-} = \frac{P_t^+}{P_r^-},\tag{2}$$

where  $T_t^+$  represents the transmission probability under forward bias from the transmission terminal t to the rejection terminal t whereas  $T_r^-$  represents the transmission probability under reverse bias from the rejection terminal t to the transmission terminal t. A billiard ball model of ballistic electron motion, t similar to our MC simulations, can be used to determine the ratio of transmission coefficients by simply calculating the analogous ratio of the probabilities of

transmission,  $P_t^+$  and  $P_r^-$ , as shown on the right-hand side of eq. 2, assuming the same number of transmission channels from either terminal. This ratio is directly provided by our MC simulations by tracking the fraction of trajectories that successfully transmit from terminal t to terminal r (and vice versa), allowing direct prediction of  $\delta$ . Figure 3B illustrates the four possible outcomes for individual charge carrier trajectories when they are injected from terminal t (I, II) or terminal r (III, IV) and either transmit through the constriction (I, III) or are rejected and scattered back to the starting terminal (II, IV). The number of carriers that successfully transmit from start terminal to end terminal of the structure in the allowed simulation time (3.3 x  $10^{-11}$  s) are divided by the total number of carriers injected from the start terminal to determine the probability of transmission.

To understand the charge carrier concentration (n), charge density ( $\rho$ ), and electric field (E) profiles in a NW GD, finite-element simulations of an n-type device were performed based on measured experimental geometries and expected dopant profiles to delineate the most likely quasi-ballistic regions of the device. Figure 4A displays a schematic of a typical dopant profile that would be encoded during the growth of Si NW diode in order to produce, after wet-chemical etching of the NW, the asymmetric geometry needed for a GD. Using this dopant profile, finite-element simulations were performed and plots of n,  $\rho$ , and E at  $V_{app} = 1$  V are shown in Figure 4B. The geometry and dopant profile produce an electric field that changes direction within the ratchet structure because of the change in the space charge density across the nanostructure. Note that the addition of a positive surface charge density to the simulations in Figure 4B results in band bending and depletion in the vicinity of the constriction, causing the effective constriction diameter d to be smaller than the physical geometry. However, the overall shape of the

conductive channel remains similar; thus, the geometries used in MC can be considered effective geometries that reflect both the physical geometry and electrostatic effects from surface charge.

Figure 4C displays the bulk Si MFP, calculated from the empirical mobility<sup>40</sup> and thermal velocity, as a function of position within the NW GD, where the MFP value is primarily limited by ionized impurity scattering based on the expected dopant concentration at each position. Because of the modulated doping within the nanostructure, the MFP peaks within the constriction and decays sharply into the rejection taper. On the side of the transmission taper, the MFP plateaus at  $\sim$ 12 nm close to the constriction and decays less rapidly into the transmission taper. Considering the MFP, E, and n distributions, we consider the most likely quasi-ballistic region to be encompassed within the dashed boxed region shown in Figure 4B, and the simulated quasi-ballistic region of the ratchet structure will generally involve quasi-ballistic transport through  $\sim$ 20 nm of the structure on both sides of the constriction.

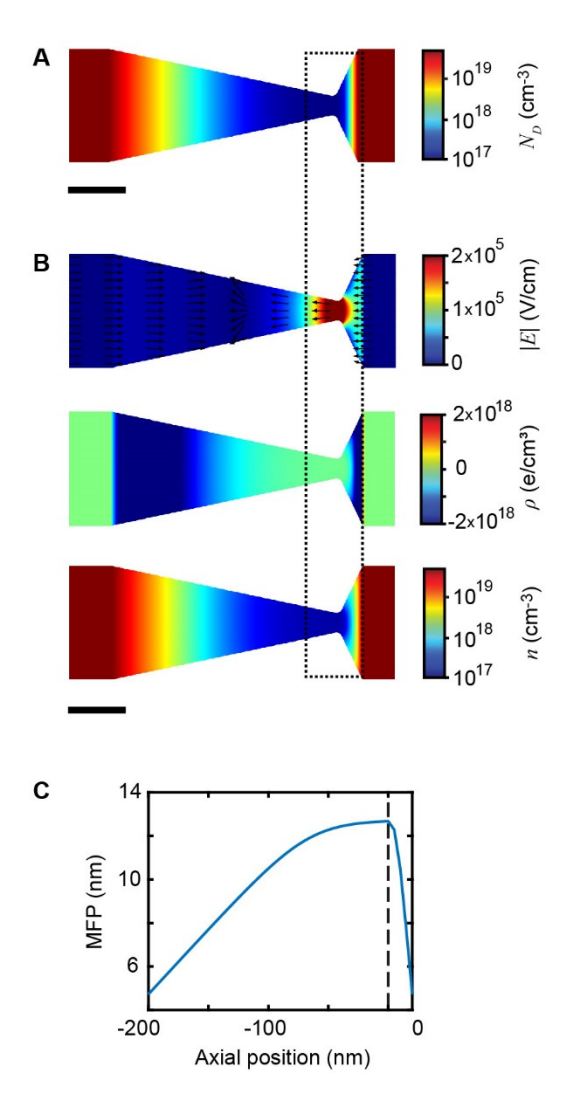


Figure 4. Electrostatics and MFP. (A) Donor dopant ( $N_D$ ) profile used in the finite-element simulation; scale bar, 40 nm. (B) Finite-element simulation results at  $V_{app} = 1$  V showing the electric field |E| with normalized field lines (top), space charge density  $\rho$  (middle), and carrier density n (bottom); scale bar, 40 nm. (C) Plot of MFP at room T as a function of axial position through the transmission and rejection tapers of the structure based on the dopant profile in panel A, with a dashed line denoting the position of the constriction.

We first consider the effect of MFP and transmission taper length on the apparent DC asymmetry,  $\delta$ . As illustrated in Figure 5A, all geometric parameters are held constant except for

the transmission taper length L, which is varied from 2 to 200 nm. For shorter L, carriers are injected into the simulation domain very close to the constriction, within the region that should behave quasi-ballistically. As L increases, carriers are injected farther from the constriction and eventually transition out of the region that should behave quasi-ballistically, increasing the likelihood of scattering events that direct carriers away from the constriction. Thus, as L increases, transport should transition from ballistic to quasi-ballistic to diffusive. On the rejection taper side, the geometry is held constant with the rejection terminal at a fixed distance l=10 nm from the constriction.

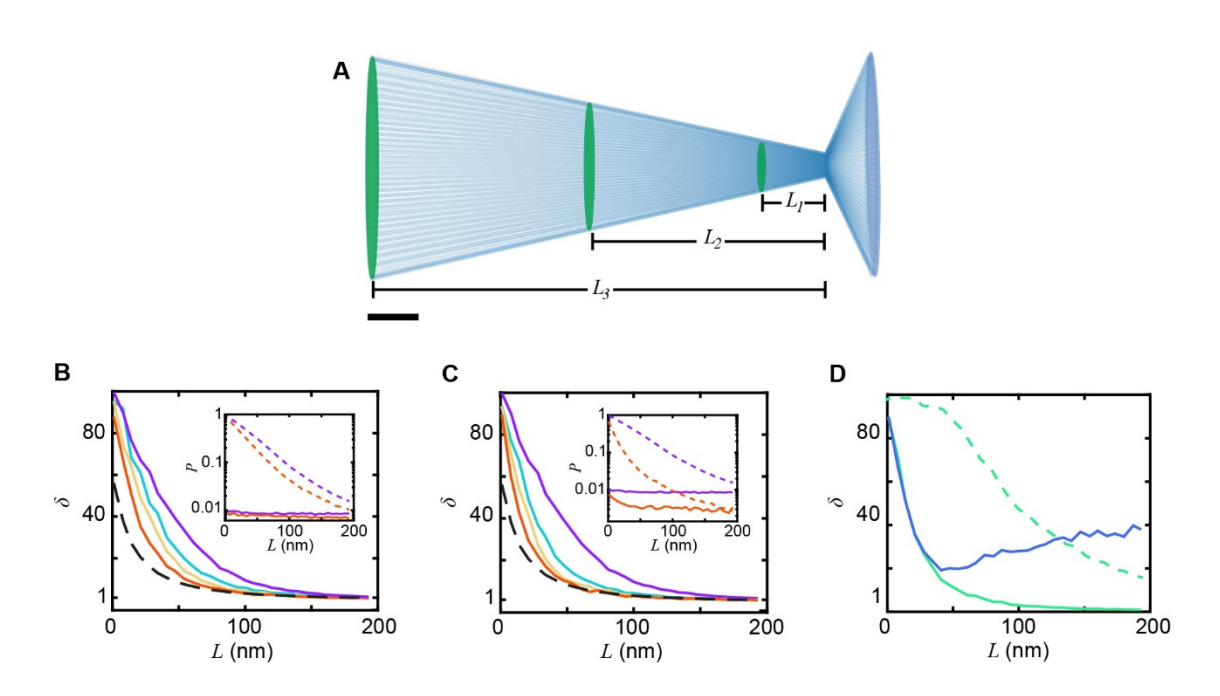


Figure 5. Effects of MFP and transmission taper length. (A) Schematic of a NW GD with varying L (denoted schematically as  $L_1$ ,  $L_2$ , and  $L_3$ ) for fixed D = 100 nm, d = 10 nm, l = 10 nm,  $\theta = 13^{\circ}$ , and  $\varphi = 77^{\circ}$ ; scale bar, 40 nm. (B, C) Plots of  $\delta$  as function of L without an electric field and with MFPs of 10 nm (orange), 20 nm (yellow), 35 nm (cyan), and 60 nm (purple) produced at constant T = 100 K and  $N_D = 10^{17}$  cm<sup>-3</sup>,  $10^{16}$  cm<sup>-3</sup>,  $10^{15}$  cm<sup>-3</sup>, and  $10^{13}$  cm<sup>-3</sup> respectively (panel B), or produced at constant  $N_D = 10^{13}$  cm<sup>-3</sup> and T = 450 K, 300 K, 200 K, and 100 K, respectively

(panel C). Insets: plots of  $P_t$  (dashed line) and  $P_r$  (solid line) for MFPs of 10 nm (orange) and 60 nm (purple). Black dashed lines represent the ratios of the transmission terminal t areas to the rejection terminal t areas. (**D**) Plot of  $\delta$  as function of t with an electric field (t = 10<sup>4</sup> V/cm) and MFP of 20 nm (blue curve), without an electric field (t = 0 V/cm) and MFP of 20 nm (cyan curve), and without an electric field (t = 0 V/cm) and without scattering (dashed cyan curve) to reflect pure ballistic transport.

Figures 5B and 5C display  $\delta$  as a function of L for electrons without an electric field and with different MFPs as determined by changing  $N_D$  at constant T or changing T at constant  $N_D$ , respectively. MFPs were varied from ~10 to ~60 nm, and both data sets show similar trends with MFP and L, with  $\delta$  approaching 1 (i.e. no difference in transmission probabilities from either side) at longer values of L. Interestingly, the impact of MFP on  $\delta$  is less pronounced than might initially be expected, with even a short MFP of ~10 nm able to produce a  $\delta$  above 20 for shorter L values. The origin of this relatively weak MFP dependence can be understood by examining the individual transmission probabilities  $P_t$  and  $P_r$  from the transmission and rejection tapers of the nanostructure, respectively, as shown in in the insets of Figure 5B,C. As apparent from these plots, the rejection taper has a uniformly low  $P_r$ , implying that the rejection taper effectively prevents electrons from passing through the constriction under all conditions. The transmission taper has a much higher  $P_t$  that relatively slowly decays as L increases. Thus, the relatively weak dependence of  $\delta$  on MFP for shorter L can be interpreted to result from the good rejection characteristics on one side but also from the relatively good transmission on the other. Plots of  $P_t$ and  $P_r$  at all values of MFP are shown in Figure S1. MFP does begin to strongly effect the GD performance at intermediate values of L, where higher MFP values enable substantially larger

values of  $\delta$ , driven by higher  $P_t$  values while  $P_r$  remains approximately constant. The results also highlight the importance of correctly identifying the quasi-ballistic region of Si NW GDs (*i.e.* choosing physical reasonable values of L) when modeling data for comparison to experimental measurements.

Figure 5D compares  $\delta$  as a function of L for MC simulations without an electric field and with a uniform electric field ( $E = 10^4 \text{ V/cm}$ ) directed along the NW axis, a value motivated by the finite-element results in Figure 3B. The axial momentum distribution is not biased when the electric field is non-zero, as the explicit electric field instead serves to bias the momentum. For simulations with zero electric field in Figure 5D, the MFP is either 20 nm (solid cyan curve) or infinite (dashed cyan curve), with the latter reflecting pure ballistic transport without scattering inside the structure. For the non-zero electric field simulation (blue curve, Figure 5D), the MFP is also 20 nm. However, regardless of MFP or electric field, the value of  $\delta$  initially decreases with increasing L. However, with an electric field,  $\delta$  begins increasing for L greater than the MFP. This effect results from the electric field redirecting electrons toward the constriction (effectively serving to inject them into the quasi-ballistic region closer to the constriction) to facilitate transmission. The electric field can compensate for short MFPs and for nontransmissive initial trajectories by mitigating the rejection of carriers on the transmission side, resulting in greater  $\delta$  values than both the short MFP and purely ballistic, infinite MFP simulations at longer L. For carriers with the same MFP, the similarity of the curves with and without an electric field for small values of L, combined with the prediction of  $\delta$  values at longer L with an electric field that are similar to the ones at shorter L, together provide further motivation to perform MC models of the NW GDs with relatively small values of L, a biased

axial momentum distribution (Figure S2), and no electric field, as done in the remainder of this work.

The MC simulation makes possible a systematic examination of the relationship between individual geometric parameters and  $\delta$ . Toward this end, we focus first on the geometry of the transmission taper (Figure 6) and then the rejection taper (Figure 7) to identify the most influential geometric trends. Figure 5A displays a heat map of  $\delta$  as a function of the geometric parameters d and  $\theta$  with D, I, and MFP fixed at 100 nm, 10 nm, and 12 nm, respectively, while L and  $\varphi$  change accordingly with  $\theta$  and d. Figures 6B,C also display heat maps of  $P_t$  and  $P_r$ , where the ratio of the data in Figure 6B and 6C produces the  $\delta$  values shown in Figure 6A. Sweeping over values for d and  $\theta$  reveals the interdependence of the parameters to determine the performance of the GD devices, as exemplified by the four geometries (Figure 6D) corresponding to the points labeled I-IV in Figures 6A-C.

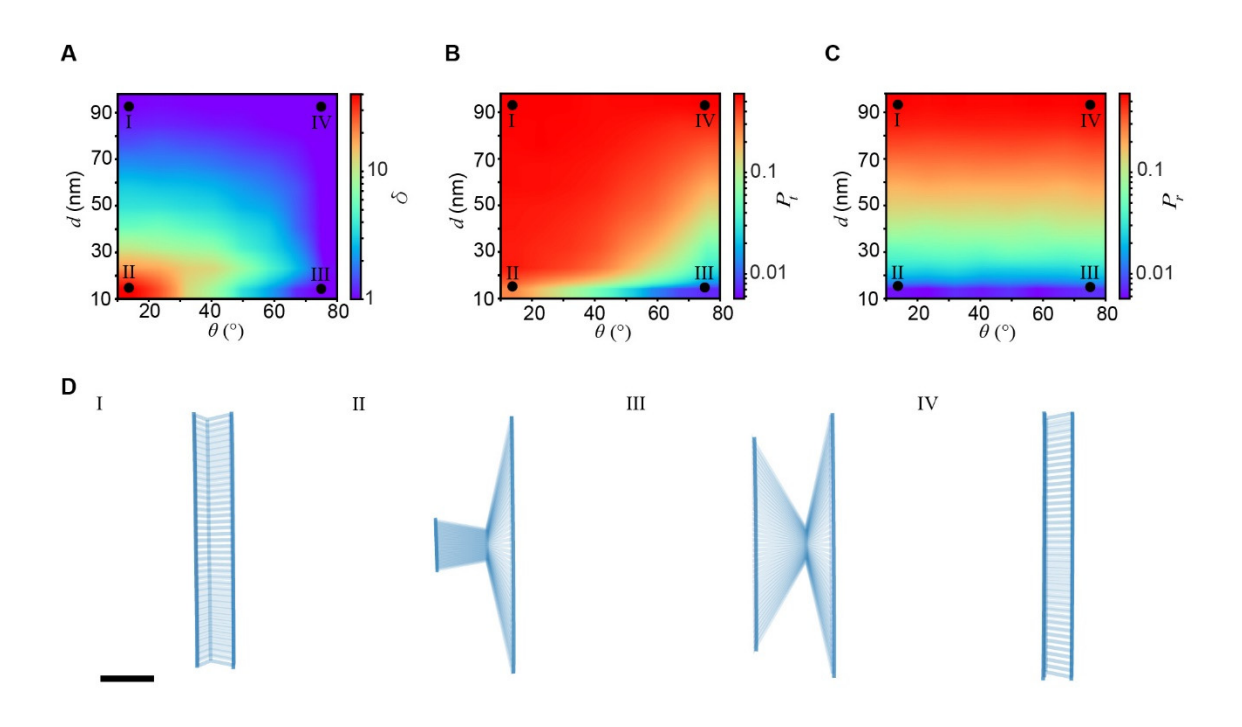


Figure 6. Transmission taper geometric effects. Heat maps of (A)  $\delta$ , (B)  $P_t$ , (C)  $P_r$  for a GD structure with varying d and  $\theta$  for fixed D = 100 nm, l = 10 nm, and MFP = 12 nm. (D) Schematics of GD geometry corresponding to the four points labeled I-IV in panels A-C; scale bar, 20 nm.

For smaller  $\theta$  angles of ~15°, the impact of the constriction diameter d is evident as  $\delta$  increases as d decreases (e.g. moving from point I to point II). The plots of  $P_t$  and  $P_r$  reveal that as d decreases the rejection taper becomes more effective at blocking carriers, while electron transmission from the transmission taper is approximately constant because the small  $\theta$  angle is highly favorable to transmission. On the rejection taper, the angle  $\varphi$  increases significantly as d decreases, causing significant back scattering of the electron and reducing  $P_r$ . This result highlights the important role of the rejection taper and high  $\varphi$  angles in improving the GD performance.

For smaller d values of  $\sim$ 15 nm, the impact of the transmission angle  $\theta$  is evident as  $\delta$  decreases from a maximum to a value of  $\sim$ 1 as  $\theta$  increases (e.g. moving from point II to point III). As apparent from the plots of  $P_t$  and  $P_r$ ,  $\delta$  decreases because  $P_t$  decreases as the transmission taper shifts from tending to direct electrons through the constriction to tending to direct them back toward the transmission terminal. On the rejection taper, the value of  $P_r$  is approximately constant. As apparent from geometries II and III in Figure 6D, the transmission taper transitions from a highly asymmetric structure at small  $\theta$  to a largely symmetric bowtie structure at large  $\theta$ , where the symmetric structure has lost the GD behavior as manifested by  $\delta \sim 1$ .

For larger  $\theta$  angles of ~75°,  $\delta$  is ~1 for all values of d (e.g. moving from point III to point IV) because the transmission taper rejects carriers by directing them away from the constriction,

just as the rejection taper does. This results in nearly identical values for  $P_t$  and  $P_r$ , indicating symmetric transport of charge carriers and absence of diode behavior. While small d (point III) results in smaller  $P_t$  and  $P_r$  values than large d (point IV), the change in both with d is approximately the same, leading to a static value of  $\delta \sim 1$ . Finally, for large values of  $d \sim 95$  nm, the NW structure is almost geometrically uniform, causing  $\delta \sim 1$  and causing all transmission probabilities to be high even for a substantial change in  $\theta$  (e.g. moving from point IV to point I). Overall, the heatmaps in Figure 6A-C highlight the importance of a small constriction d, small transmission taper angle  $\theta$ , and large rejection taper angle  $\varphi$  to achieve asymmetric charge carrier transport, expressed quantitatively as a large  $\delta$  value.

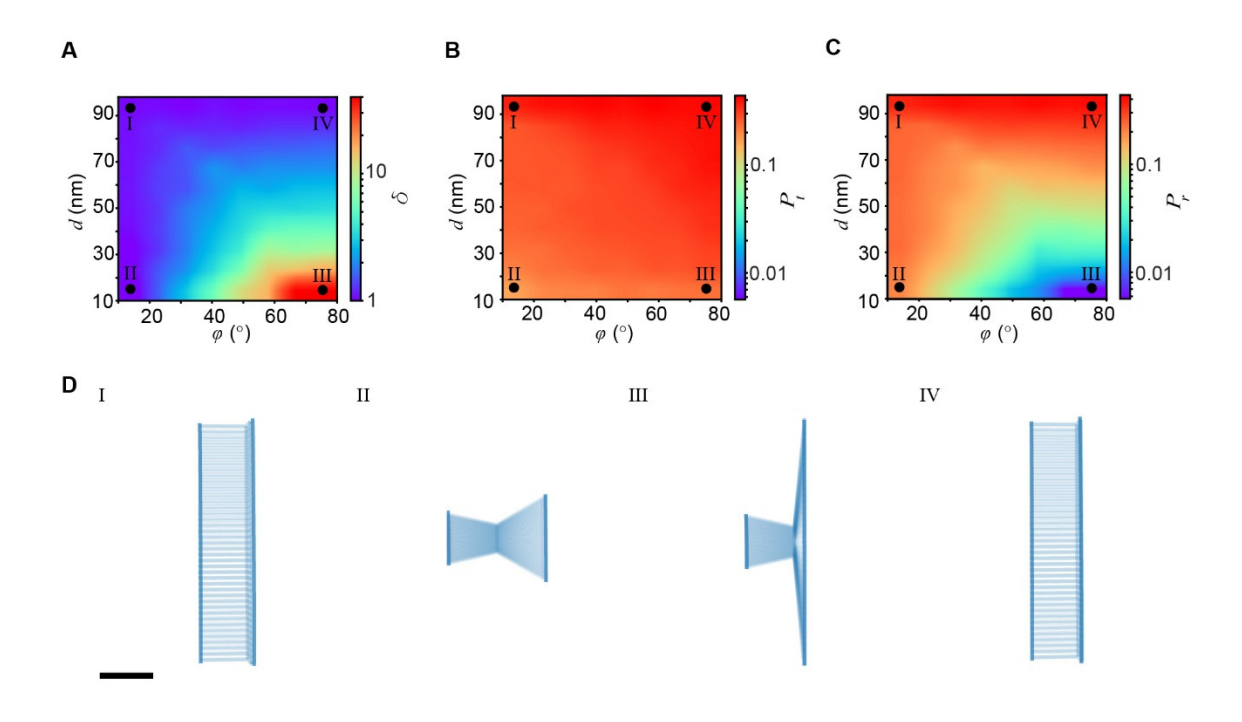


**Figure 7. Rejection taper geometric effects.** Heat maps of (**A**)  $\delta$ , (**B**)  $P_t$ , and (**C**)  $P_r$  for a GD structure with varying d and  $\varphi$  for fixed D = 100 nm, L = 20 nm, and MFP = 12 nm. (**D**)

Schematics of GD geometry corresponding to the four points labeled I-IV in panels A-C; scale bar, 20 nm.

Analogous to Figure 6, Figure 7 displays GD MC data as a function of the parameters d and  $\varphi$  with D, L, and MFP fixed at 100 nm, 200 nm, and 12 nm, respectively, while l and  $\theta$  change accordingly with  $\varphi$  and d. Figure 7A displays a heat map of  $\delta$  while Figures 7B,C display heat maps of  $P_t$  and  $P_r$ . Four exemplary geometries, denoted I-IV, are shown in Figure 7D. For smaller  $\varphi$  angles of ~15°,  $\delta$  is ~1 for all values of d (e.g. from point I to point II) because, just like the transmission taper, the rejection taper transmits carriers by directing them toward the constriction, as indicated by the nearly identical values of  $P_t$  and  $P_r$ . The larger d geometries (e.g. point I) result in slightly larger  $P_t$  and  $P_r$  values than smaller d (e.g. point II) because the majority of carriers pass through the large constriction without reflecting off the structure, making them more likely to successfully transmit without back scattering.

For smaller d values of ~15 nm,  $\delta$  increases from ~1 to the maximum value as  $\varphi$  increases (e.g. from points II to III) because the transmission taper transitions from directing carriers toward the constriction to reflecting them away, leading to a decreasing  $P_r$  while  $P_t$  stays approximately constant. The geometries corresponding to points II and III (Figure 7D) highlight how the transmission taper remains unchanged while the rejection taper transitions from an approximately symmetric bowtie structure to an asymmetric structure that is able to effectively direct carriers away from the constriction.

For larger  $\varphi$  angles of ~75°,  $\delta$  decreases as d increases (e.g. moving from points III to IV), changing from the maximum value to ~1. The expanding constriction d becomes less effective at blocking carriers on the rejection side, leading to an increasing  $P_r$  while  $P_t$  remains

approximately constant. Finally, for large values of  $d \sim 95$  nm, the NW structure is almost geometrically uniform, causing  $\delta \sim 1$  and causing all transmission probabilities to be high even for a substantial change in  $\varphi$  (e.g. moving from point IV to point I). In general, these heatmaps highlight the importance of a small constriction d and large rejection taper angle  $\varphi$  to achieve a large  $\delta$ .

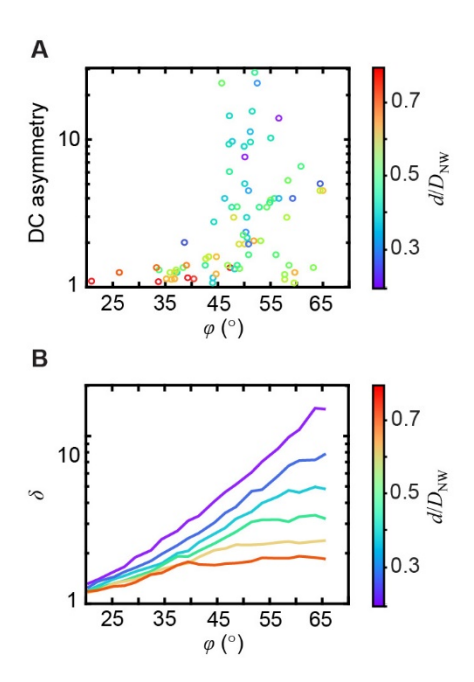


**Figure 8. Comparison of Simulation and Experiment.** (**A**) Plot of the experimental values of DC asymmetry at  $|V_{app}| = 1$  V collected from 81 single-NW devices plotted as a function of the rejection taper angle  $\varphi$  for different ratios,  $d/D_{\rm NW}$ , of constriction diameters, d, to NW outer diameter,  $D_{\rm NW}$ . Data was replotted from reference 34. (**B**) Plot of  $\delta$  from MC simulations as a function of  $\varphi$  for different ratios of constriction diameters to NW diameters ( $d/D_{\rm NW} = 0.2, 0.3, 0.4, 0.5, 0.6,$  and 0.7 for purple through red curves, respectively) with fixed D = 100 nm, L = 20 nm, and MFP = 12 nm.

As observed in experimental measurements (Figure 2) and predicted by MC simulations (Figures 6,7), the  $\varphi$  angle of the rejection taper and the constriction diameter have significant impacts on  $\delta$ . As  $\varphi$  increases,  $\delta$  increases, and this trend is accentuated for structures with small d values. Notably, the experimental results in Figure 2C show an increase in asymmetry and decrease in current for GD structures with increased  $\varphi$  and decreased d values. Qualitatively, we observe these same trends in  $\delta$  and  $P_t$  in Figures 6A,B in  $\delta$  and  $P_r$  in Figures 7A,C. To further verify these ballistic trends, we compare simulation results to experimental measurements on Si NW GDs. 34 Devices presented here (Figure 2) and from past experimental measurements 34 are identical in fabrication and measurement procedures. Replotting the experimental data reported in reference 34, Figure 8A correlates Si NW GD  $\varphi$  angles with experimentally measured DC asymmetry  $\delta$  values measured at  $|V_{app}| = 1$  V, showing more than an order of magnitude increase as  $\varphi$  increases. The data are color-coded by the ratio of constriction diameter to NW diameter,  $d/D_{\rm NW}$ . For a majority of the measured structures, DC asymmetry increases as  $d/D_{\rm NW}$  decreases. Figure 8B plots analogous data from MC simulations for  $\delta$  as a function of  $\varphi$  for several values of  $d/D_{\rm NW}$ . Similar to the experimental data, the trend of increasing  $\delta$  with increasing  $\varphi$  is present for all  $d/D_{NW}$  ratios, and it plays a more significant role as  $d/D_{NW}$  decreases because both the transmission and rejection tapers are better able to direct carrier transport to yield diode behavior. The good qualitative agreement between the experimental data in Figure 8A and MC simulations in Figure 8B support the quasi-ballistic characteristics of the experimental Si NW GDs and demonstrate that the MC methods and design principles described herein reproduce key aspects of the GD performance.

#### **CONCLUSION**

In this work, we develop a MC simulation of quasi-ballistic Si NW GDs to clarify the experimentally observed relationship between NW GD geometry and device performance. Through this model, we establish design principles that relate the physical geometry, temperature (T), and dopant concentration ( $N_D$ ) to  $\delta$ . Modeling charge carrier paths through the GD structure revealed the importance of carrier MFP (determined by T and  $N_D$ ), specular reflection at surfaces, and geometry to quasi-ballistic transport under various conditions. Geometry is the most influential factor, with the angles of the transmission and rejection tapers determining the nanostructure's effectiveness in directing and blocking charge carriers. The constriction size strongly modulates the angles and affects carrier interactions with the boundaries of the GD. Under ideal geometric conditions, the structure has a small  $\theta$  angle, large  $\varphi$  angle, and small  $d/D_{\rm NW}$  ratio, and the blocking effect is at least as important as the directing effect in achieving asymmetric carrier transport. The importance of this blocking effect and the relative short associated length scales leads to relative weak dependence of GD performance on charge carrier MFP. These MC simulation results enable prediction and interpretation of experimental trends and can be used to direct NW GD design and fabrication. They clarify the mechanism of quasiballistic transport in NW GDs and can enable progress toward achieving THz rectification with these structures.

#### **METHODS**

Nanowire Synthesis and Etching. Si NWs were synthesized from Au nanoparticle catalysts by a vapor-liquid-solid (VLS) mechanism in a home-built, hot-wall chemical vapor deposition (CVD) system.<sup>36</sup> Silane (SiH<sub>4</sub>; Voltaix) was used as the source of Si and phosphine (PH<sub>3</sub>; 1000 ppm PH<sub>3</sub> in H<sub>2</sub>; Voltaix) as the source of P for n-type doping, with hydrogen (H<sub>2</sub>;

Matheson TriGas 5 N semiconductor grade) as the carrier gas. Growth substrates, 1 x 2 cm Si wafers (NOVA Electronic Materials, (100) p-type Si with 600 nm thermal oxide), were functionalized with poly-L-lysine (Sigma-Aldrich) and citrate-stabilized 100 nm diameter Au catalysts (Ted Pella) and then inserted into the center a single-zone 1-inch tube furnace (Lindberg BlueM). NWs were nucleated for 15 minutes at 440-450 °C with 200 standard cubic centimeter per minute (sccm) H<sub>2</sub> and 2.00 sccm SiH<sub>4</sub> at 40 torr total reactor pressure. After nucleation, the temperature was ramped to 420 °C over 15 minutes, the PH<sub>3</sub> flow was set to 20 sccm, the total reactor pressure was ramped to 20 torr, and the H<sub>2</sub> flow was ramped to 100 sccm over 1 minute. The first degenerately doped n-type section was grown by maintaining the PH<sub>3</sub> flow of 20 sccm for 60 minutes. The sawtooth geometry was encoded in the NW by controllably ramping the PH<sub>3</sub> flow from 20 to 0 sccm in steps with a duration of 3 seconds or more each and then the flow rate was held at 0 sccm for 15 seconds to create the transmission taper of the ratchet, and then abruptly returned to 20 sccm to create the rejection taper. Following the sawtooth, second degenerately doped n-type section was encoded by again maintaining the PH<sub>3</sub> flow at 20 sccm for 60 minutes. Based on dopant flow profile, the minimum doping level in the ratchet section, near the constriction, is likely below 10<sup>18</sup> cm<sup>-3</sup> due to suppression of the reservoir effect. 41-43 To achieve the desired physical geometry, NWs were mechanically dry transferred to device substrates, etched in buffered hydrofluoric acid (BHF, ~5% by volume) for ~10 seconds to remove the surface oxide, and dopant-selectively etched with room-temperature aqueous KOH solution (20% by weight) for 120-240 seconds.

**Device Fabrication.** Marker patterns were fabricated on device substrates, (100) p-type Si wafers with 100 nm of thermal oxide and 200 nm Si<sub>3</sub>N<sub>4</sub>, by etching into the wafer with a spun photo-resist stack (3 layers of MMA; MicroChem (8.5) EL9, 1 layer of (PMMA; MicroChem

950PMMA.A7) with electron-beam lithography (EBL) using an FEI Helios 600 Nanolab Dual Beam System with Nanometer Pattern Generation System (NPGS) and deep reactive ion etching (DRIE; Alcatel AMS 100). Contacts to the NW were defined by spinning a photo-resist stack (2 layers of MMA; MicroChem (8.5) EL9, 1 layer of (PMMA; MicroChem 950PMMA.A2) onto device substrates with etched NWs and using EBL with NPGS. Device substrates were then developed, etched in BHF for 10 seconds, and metal contacts were fabricated by electron-beam evaporation (Kurt Lesker PRO Line PVD75) of 3 nm of Ti and 150-200 nm of Pd.

**Device Measurements.** Single-NW device measurements were performed at room temperature and in the dark, using a probe station (Lakeshore TTPX Cryogenic Probe Station), under vacuum (<5 mTorr) and a source measure unit (SMU, Keithley 2636B) with triax cable connections (Belden 9222 50  $\Omega$ ).

**Electron Microscopy.** SEM was performed with an FEI Helios 600 Nanolab Dual Beam System with an imaging resolution of less than 5 nm.

**Finite-element modeling.** Finite-element simulations using COMSOL Multiphysics have been previously employed to study the electrostatic nature of NW GDs.<sup>34</sup> The finite-element model employed here includes Poisson's equation, explicit dopant profiles, drift-diffusion with density-dependent electrical mobilities and diffusion constants, bandgap renormalization, and Shockley-Read-Hall, Auger, and surface recombination, as described previously.<sup>36</sup>

MC model. Our MC model follows a standard model for Si and an algorithm outlined by Lundstrom, further details are in the Supporting Information.<sup>39</sup> It considers four types of energy-dependent electron scattering processes, including acoustic deformation potential scattering, equivalent intervalley scattering by phonon absorption and emission, and ionized impurity scattering.

Considering the *T*-dependent electrical mobility of Si, we note that mobility is proportional to  $T^{3/2}$  at low temperatures (T < 350 K), where impurity scattering mechanisms are dominant, and proportional to  $T^{-3/2}$  at high temperatures (T > 350 K), where lattice scattering mechanisms are dominant. Because the scattering rate is well characterized at T = 300 K, we scaled the ionized impurity scattering rate by a factor of (T/300 K) $^{3/2}$  and the scattering rates due to lattice mechanisms by (T/300 K) $^{-3/2}$ . This successfully reproduced the general trend in experimental results for the *T*-dependent electrical mobility of Si,  $^{40}$  as shown in Figure S3, where electrical mobility was calculated from simulated carrier MFPs at different values of *T* and  $N_D$ .

To simulate a NW GD device, we introduce boundaries that represent the NW physical geometry as two 3D cartesian (x, y, z) cones with offset vertices, where each cone can be expressed as:

$$y^2 + z^2 = a^2(x - x_v)^2,$$
 (3)

with the x-axis as the central axis, the vertex at position ( $x_v$ , 0, 0), and a, the slope of the cone. The vertex positions  $x_v$  and slopes a of two cones are varied to represent distinct GD geometries. We consider the boundaries to be idealized surfaces that are atomically smooth and defect free. At surface boundaries, we assume elastic scattering can be described as specular reflection at the point of intersection between the charge carrier and surface; thus, the momentum vector after reflection,  $p_{ref}$ , is calculated as:

$$\boldsymbol{p}_{\text{ref}} = \boldsymbol{p} - 2proj(\boldsymbol{p}, \boldsymbol{N}), \tag{4}$$

where N is the normal vector to the surface at the point of reflection and proj(p,N) is the vector projection of p onto N. We assume a surface boundary reflection is probabilistically independent from a scattering event in the bulk, so the charge carriers continue their trajectories after reflection until the next scattering event predicted by the model.

The model requires identification of the points of intersection of a carrier trajectory with the physical boundary. As shown in the Supporting Information, combining the equation of motion of the charge carrier with the expressions (eq. 3) for the surface boundary leads to a quartic expression for the time points at which an intersection will occur. Solving for the resulting roots of the expression yields solutions that are then filtered to identify the first non-imaginary, physically reasonable intersection (*i.e.* ones that represent the temporally first intersection with a physically valid portion of a cone at a time point less than the free flight time of the trajectory).

To start a trajectory, a charge carrier is injected into the quasi-ballistic region from either termination plane by randomly selecting the start position from a uniform positional distribution across the circular cross section. The starting momentum of the carrier is determined by selecting non-axial momentum components from a Gaussian with mean  $\mu=0$  and standard deviation  $\sigma=\sqrt{m^*k_BT}$ , where the axial component  $p_{axial}=\sqrt{-2m^*k_BT\ln(r_{axial})}$  is specified by selecting a random number  $r_{axial}$  from a uniform distribution from 0 to  $1.^{39}$  The axial momentum distribution is biased by an applied voltage,  $V_{app}$ , of 1 V by adding  $\sqrt{2m^*eV_{app}}$  to the axial momentum, resulting in a shift of the probability density ( $P(v_{axial})$ ) for the initial carrier axial velocity ( $v_{axial}$ ), as shown in Figure S2. To end a trajectory, a charge carrier within the radial bounds of the geometry must intersect either termination plane. For simplicity, the MC simulation domain is assumed to have a uniform dopant concentration. The quasi-ballistic region therefore has a constant MFP and is constructed by placing the transmission and rejection terminals within approximately one MFP of the constriction. We assume there is negligible flux against the potential gradient.

ASSOCIATED CONTENT

Supporting Information Available. Model theory and development, probabilities of

transmission for ballistic simulations with various electron MFPs, simulated electron mobility,

and initial electron axial velocity plots are provided in Supporting Information. This material is

available free of charge on the ACS Publications website at http://pubs.acs.org.

**AUTHOR INFORMATION** 

**Corresponding Author** 

\*Email: jfcahoon@unc.edu.

**Notes** 

The authors declare no competing financial interest.

**ACKNOWLEDGMENTS** 

This work was funded by the National Science Foundation (NSF) under grant CBET-1914711

and ECCS-2201292 and by a Packard Fellowship for Science and Engineering. This work made

use of instrumentation at the Chapel Hill Analytical and Nanofabrication Laboratory (CHANL),

a member of the North Carolina Research Triangle Nanotechnology Network (RTNN), which is

supported by the NSF (ECCS-2025064) as part of the National Nanotechnology Coordinated

Infrastructure (NNCI).

**REFERENCES** 

Lau, B.; Kedem, O., Electron ratchets: State of the field and future challenges. J. Chem. Phys. 2020,

*152* (20), 200901.

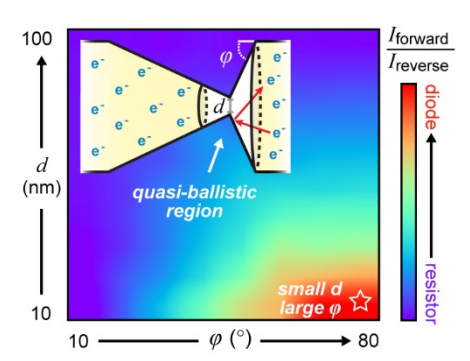
28

- 2. Lau, B.; Kedem, O.; Schwabacher, J.; Kwasnieski, D.; Weiss, E. A., An introduction to ratchets in chemistry and biology. *Mater. Horiz.* **2017**, *4* (3), 310-318.
- 3. Reimann, P., Brownian motors: noisy transport far from equilibrium. *Phys. Rep.* **2002**, *361* (2), 57-265.
- 4. Linke, H.; Song, A. M., Electron ratchets—nonlinear transport in semiconductor dot and antidot structures. In *Electron Transport in Quantum Dots*, Bird, J. P., Ed. Springer US: Boston, MA, 2003; pp 317-361.
- 5. Hoffmann, P. M., How molecular motors extract order from chaos (a key issues review). *Rep. Prog. Phys.* **2016**, *79* (3), 032601.
- 6. Browne, W. R.; Feringa, B. L., Making molecular machines work. *Nat. Nanotechnol.* **2006,** *I* (1), 25-35.
- 7. Loutherback, K.; Puchalla, J.; Austin, R. H.; Sturm, J. C., Deterministic microfluidic ratchet. *Phys. Rev. Lett.* **2009**, *102* (4), 045301.
- 8. Rousselet, J.; Salome, L.; Ajdari, A.; Prostt, J., Directional motion of brownian particles induced by a periodic asymmetric potential. *Nature*. **1994**, *370* (6489), 446-447.
- 9. Brillouin, L., Can the Rectifier Become a Thermodynamical Demon? *Phys. Rev.* **1950**, 78 (5), 627-628.
- 10. Lorke, A.; Wimmer, S.; Jager, B.; Kotthaus, J. P.; Wegscheider, W.; Bichler, M., Far-infrared and transport properties of antidot arrays with broken symmetry. *Physica B* **1998**, *249-251*, 312-316.
- 11. Song, A. M.; Lorke, A.; Kriele, A.; Kotthaus, J. P.; Wegscheider, W.; Bichler, M., Nonlinear electron transport in an asymmetric microjunction: A ballistic rectifier. *Phys. Rev. Lett.* **1998**, *80*, 3831-3834.
- 12. Linke, H.; Humphrey, T. E.; Lofgren, A.; Sushkov, A. O.; Newbury, R.; Taylor, R. P.; Omling, P., Experimental tunneling ratchets. *Science*. **1999**, *286* (5448), 2314-7.
- 13. Linke, H.; Sheng, W. D.; Svensson, A.; Löfgren, A.; Christensson, L.; Xu, H. Q.; Omling, P.; Lindelof, P. E., Asymmetric nonlinear conductance of quantum dots with broken inversion symmetry. *Phys. Rev. B* **2000**, *61* (23), 15914-15926.
- 14. Linke, H.; Humphrey, T. E.; Taylor, R. P.; Taylor, R. P.; Micolich, A. P.; Micolich, A. P.; Newbury, R., Chaos in Quantum Ratchets. *Phys. Scr.* **2001**, *T90* (1), 54.
- 15. Song, A. M.; Omling, P.; Samuelson, L.; Seifert, W.; Shorubalko, I.; Zirath, H., Room-temperature and 50 GHz operation of a functional nanomaterial. *Appl. Phys. Lett.* **2001**, *79* (9), 1357-1359.
- 16. Song, A. M., Electron ratchet effect in semiconductor devices and artificial materials with broken centrosymmetry. *Appl. Phys. A* **2002**, *75*, 229-235.
- 17. Müller, T.; Würtz, A.; Lorke, A.; Reuter, D.; Wieck, A. D., Wave-form sampling using a driven electron ratchet in a two-dimensional electron system. *Appl. Phys. Lett.* **2005**, *87* (4), 042104.
- 18. Sassine, S.; Krupko, Y.; Portal, J. C.; Kvon, Z. D.; Murali, R.; Martin, K. P.; Hill, G.; Wieck, A. D., Experimental investigation of the ratchet effect in a two-dimensional electron system with broken spatial inversion symmetry. *Phys. Rev. B* **2008**, *78* (4), 045431.
- 19. Kannan, E. S.; Bisotto, I.; Portal, J. C.; Beck, T. J.; Jalabert, L., Energy free microwave based signal communication using ratchet effect. *Appl. Phys. Lett.* **2012**, *101* (14), 143504.
- 20. Tanaka, T.; Nakano, Y.; Kasai, S., GaAs-Based Nanowire Devices with Multiple Asymmetric Gates for Electrical Brownian Ratchets. *Jpn. J. Appl. Phys.* **2013**, *52* (6S), 06GE07.
- 21. Zhang, P.; Hung, D. M. H., An analytical model for ballistic diode based on asymmetric geometry. *J. Appl. Phys.* **2014**, *115* (20), 204908.
- 22. Drexler, C.; Tarasenko, S. A.; Olbrich, P.; Karch, J.; Hirmer, M.; Müller, F.; Gmitra, M.; Fabian, J.; Yakimova, R.; Lara-Avila, S.; Kubatkin, S.; Wang, M.; Vajtai, R.; Ajayan, P. M.; Kono, J.; Ganichev, S. D., Magnetic quantum ratchet effect in graphene. *Nat. Nanotechnol.* **2013**, *8* (2), 104-107.

- 23. Zhu, Z. X.; Joshi, S.; Moddel, G., High performance room temperature rectenna IR detectors using graphene geometric diodes. *IEEE J. Sel. Top. Quantum Electron.* **2014**, *20* (6), 3801409.
- 24. Auton, G.; Zhang, J.; Kumar, R. K.; Wang, H.; Zhang, X.; Wang, Q.; Hill, E.; Song, A., Graphene ballistic nano-rectifier with very high responsivity. *Nat. Commun.* **2016,** *7*, 11670.
- 25. Zhu, Z.; Joshi, S.; Grover, S.; Moddel, G., Geometric diodes for optical rectennas. In *Rectenna Solar Cells*, Moddel, G.; Grover, S., Eds. Springer: New York, 2013; pp 209-227.
- 26. Auton, G.; But, D. B.; Zhang, J.; Hill, E.; Coquillat, D.; Consejo, C.; Nouvel, P.; Knap, W.; Varani, L.; Teppe, F.; Torres, J.; Song, A., Terahertz Detection and Imaging Using Graphene Ballistic Rectifiers. *Nano Lett.* **2017**, *17* (11), 7015-7020.
- 27. Zhang, J.; Brownless, J.; Song, A. In *High Performance Graphene Ballistic Rectifiers for THz detection*, 2019 44th International Conference on Infrared, Millimeter, and Terahertz Waves (IRMMW-THz), 1-6 Sept. 2019; 2019; pp 1-2.
- 28. Auton, G.; But, D.; Zhang, J.; Hill, E.; Coquillat, D.; Conseio, C.; Nouvel, P.; Knap, W.; Varani, L.; Teppe, F.; Torres, J.; Song, A. In *Graphene ballistic rectifiers for THz detection and imaging*, 2018 43rd International Conference on Infrared, Millimeter, and Terahertz Waves (IRMMW-THz), 9-14 Sept. 2018; 2018; pp 1-2.
- 29. Landauer, R., Conductance from transmission: common sense points. *Phys. Scr.* **1992**, *T42*, 110-114.
- 30. Landauer, R., Spatial Variation of Currents and Fields Due to Localized Scatterers in Metallic Conduction. *IBM J. Res. Dev.* **1957**, *I* (3), 223-231.
- 31. Büttiker, M.; Imry, Y.; Landauer, R.; Pinhas, S., Generalized many-channel conductance formula with application to small rings. *Phys. Rev. B* **1985**, *31* (10), 6207-6215.
- 32. Beenakker, C. W. J.; Van Houten, H., Billiard model of a ballistic multiprobe conductor. *Phys. Rev. Lett.* **1989**, *63* (17), 1857-1860.
- 33. Büttiker, M., Four-Terminal Phase-Coherent Conductance. *Phys. Rev. Lett.* **1986**, *57* (14), 1761-1764.
- 34. Custer, J. P.; Low, J. D.; Hill, D. J.; Teitsworth, T. S.; Christesen, J. D.; McKinney, C. J.; McBride, J. R.; Brooke, M. A.; Warren, S. C.; Cahoon, J. F., Ratcheting quasi-ballistic electrons in silicon geometric diodes at room temperature. *Science*. **2020**, *368* (6487), 177-180.
- 35. Tonouchi, M., Cutting-edge terahertz technology. Nat. Photon. 2007, 1 (2), 97-105.
- 36. Christesen, J. D.; Pinion, C. W.; Grumstrup, E. M.; Papanikolas, J. M.; Cahoon, J. F., Synthetically encoding 10 nm morphology in silicon nanowires. *Nano Lett.* **2013**, *13* (12), 6281-6.
- 37. Song, A. M., Formalism of nonlinear transport in mesoscopic conductors. *Phys Rev B* **1999**, *59* (15), 9806-9809.
- 38. Jacoboni, C.; Canali, C.; Ottaviani, G.; Alberigi Quaranta, A., A review of some charge transport properties of silicon. *Solid-State Electron.* **1977**, *20* (2), 77-89.
- 39. Lundstrom, M., *Fundamentals of Carrier Transport*. 2 ed.; Cambridge University Press: Cambridge, 2000.
- 40. Beadle, W. E.; Tsai, J. C. C.; Plummer, R. D., *Quick Reference Manual for Silicon Integrated Circuit Technology*. Wiley: New York, 1985; p 724.
- 41. Christesen, J. D.; Pinion, C. W.; Zhang, X.; McBride, J. R.; Cahoon, J. F., Encoding abrupt and uniform dopant profiles in vapor–liquid–solid nanowires by suppressing the reservoir effect of the liquid catalyst. *ACS Nano* **2014**, *8* (11), 11790-11798.
- 42. Ritchie, E. T.; Hill, D. J.; Mastin, T. M.; Deguzman, P. C.; Cahoon, J. F.; Atkin, J. M., Mapping free-carriers in multijunction silicon nanowires using infrared near-field optical microscopy. *Nano Lett.* **2017**, *17* (11), 6591-6597.

- 43. Kim, S.; Hill, D. J.; Pinion, C. W.; Christesen, J. D.; McBride, J. R.; Cahoon, J. F., Designing morphology in epitaxial silicon nanowires: The role of gold, surface chemistry, and phosphorus doping. *ACS Nano* **2017**, *11* (5), 4453-4462.
- 44. Sze, S. M.; Ng, K. K., *Physics of Semiconductor Devices*. 3rd ed.; John Wiley & Sons, Inc: Hoboken, NJ, 2007.
- 45. Datta, S., *Lessons from nanoelectronics : a new perspective on transport*. World Scientific Publishing Co.: Singapore ; Hackensack, NJ, 2012; p xvi, 473 p.

## For Table of Contents Only



# Supporting Information for:

# Influence of Geometry on Quasi-Ballistic Behavior in Silicon Nanowire Geometric Diodes

Kelly L. White<sup>†</sup>, Max A. Umantsev<sup>†</sup>, Jeremy D. Low, James P. Custer Jr., and James F. Cahoon\*

\* corresponding author: <u>jfcahoon@unc.edu</u>

† K.W. and M.U. contributed equally to this paper.

Department of Chemistry, University of North Carolina at Chapel Hill, Chapel Hill, NC 27599-3290, USA.

# **Supporting information includes:**

- I. Supporting TextEquations S1-S20
- II. Supporting FiguresFigures S1-S3

### I. Supporting Text

The scattering mechanisms and their associated scattering rate equation are:

1. acoustic deformation potential (ADP):

$$\frac{1}{\tau_1} = (2 \times 10^{13}) \sqrt{\frac{E(\mathbf{p})}{q}}$$
 (S1)

2. equivalent intervalley scattering by phonon absorption:

$$\frac{1}{\tau_2} = (1.5 \times 10^{13}) \sqrt{\frac{E(\mathbf{p})}{q} + .050}$$
 (S2)

3. equivalent intervalley scattering by phonon emission:

$$\frac{1}{\tau_3} = (1 \times 10^{14}) \sqrt{\frac{E(\mathbf{p})}{q} - .050}$$
 (S3)

4. ionized impurity scattering:

$$\frac{1}{\tau_4} = \left(1 \times 10^{13}\right) \left(\frac{N_I}{10^{16}}\right)^{\frac{1}{3}} \sqrt{\frac{E(\mathbf{p})}{q}} , \qquad (S4)$$

where  $\tau$  is the free-flight time associated with each scattering event,  $\mathbf{p}$ , E, and q, respectively, are the momentum, energy, and charge of the carrier, and  $N_I$  is the total concentration of ionized impurities per cubic centimeter.

The sum of the rates due to these mutually independent processes is the total scattering rate,  $\Gamma(\mathbf{p})$ , where

$$\Gamma(\boldsymbol{p}) = \sum_{i=1}^{4} \frac{1}{\tau_i} \,, \tag{S5}$$

which, after repeatedly sampling from possible carrier trajectories, determines the average freeflight duration of a carrier between scattering events. Due to its dependence on carrier energy, which varies over time, the total scattering rate,  $\Gamma(p)$ , is actually a function of time,  $\Gamma(p(t))$ , which is approximated as a(n) (arbitrary, user-defined) constant,  $\Gamma_0$ , in order to simplify derivations and reduce computational expenses. In order to yield a result that can be used to model real semiconductors, in addition to the k real scattering types, a fictitious *self-scattering* type is considered, where

$$\frac{1}{\tau_{k+1}} = \Gamma_{\text{self}}(\boldsymbol{p}) = \Gamma_0 - \Gamma(\boldsymbol{p}) > 0.$$
 (S6)

A single free flight and scattering event is simulated by generating four random numbers:  $r_1$ ,  $r_2$ ,  $r_3$ ,  $r_4$ , where each number is selected from a uniform distribution from 0 to 1.  $r_1$  is used in conjunction with  $\Gamma_0$  to determine the free-flight time until the next scattering event (real or self-scattering):

$$t_c = -\frac{1}{\Gamma_0} \ln(r_1),\tag{S7}$$

where  $t_c$  is the free-flight time between scattering events. The flight time is used to determine the position and momentum of the carrier just before the next scattering event, in accordance with Newton's law,

$$\frac{d^2\mathbf{r}}{dt^2} = \frac{q}{m^*} \mathcal{E},\tag{S8}$$

where r is position, m\* is effective mass  $(0.26m_e)$ , and  $\mathcal{E}$  is the electric field.

The scattering type is identified by comparing  $r_2$  to the partial sums of the fractional contributions of all k+1 scattering mechanisms to the total scattering rate, and selecting mechanism j if:

$$\frac{\sum_{i=1}^{j-1} \Gamma_i}{\Gamma_0} \le r_2 < \frac{\sum_{i=1}^{j} \Gamma_i}{\Gamma_0}, \qquad j = 1, 2, \dots, k+1,$$
 (S9)

where  $\Gamma_i$  is the i-th scattering mechanism. If the scattering type is self-scattering, the simulation determines a new free-flight time and the carrier continues on its current trajectory without interruption.

When a real scattering mechanism is selected, the final momentum state after scattering may change in magnitude, which is determined by the energy change  $\Delta E$  associated with the scattering mechanism, and orientation, which is determined by r<sub>3</sub> and r<sub>4</sub>. Assuming a spherical parabolic energy band, the magnitude of the momentum immediately after scattering is:

$$p(t_c^+) = p' = \sqrt{2m^*[E(t_c^-) + \Delta E]},$$
 (S10)

where  $t_c^+$  is the time at the instant after a scattering event and  $t_c^-$  is the time at the instant before a scattering event. In order to determine the new orientation, we can simplify our calculations by considering a rotated coordinate system where the primary axis is now directed along the initial momentum, the azimuthal angle  $\beta$  and the polar angle  $\alpha$  (with respect to the primary axis which is not necessarily the z-axis are determined by:

$$\beta = 2\pi r_3 \tag{S11}$$

and

$$\cos(\alpha) = 1 - 2r_4. \tag{S12}$$

In the rotated coordinate system where the x-axis is pointing along the initial momentum, the momentum vector is:

$$\mathbf{p}_r' = p' \begin{pmatrix} \cos(\alpha) \\ \sin(\alpha)\cos(\beta) \\ \sin(\alpha)\sin(\beta) \end{pmatrix}. \tag{S13}$$

Simply apply the inverse of the coordinate system rotation transformation operator to the rotated final momentum vector in order to return to the original coordinate system. This process

is repeated until an arbitrary simulation condition is satisfied (i.e. a number of real scattering events or a maximum carrier flight time).

As a carrier trajectory is entirely deterministic between scattering events, it is simple to identify the point of intersection of a carrier trajectory with a boundary if the surface is well-defined and locally continuous (smooth) in the region. Solving Equation 8 yields an equation for the trajectory of a carrier between scattering events:

$$r(0 \le t < t_c) = r_0 + \frac{p_0}{m^*} t + \frac{q\mathcal{E}}{2m^*} t^2,$$
 (S14)

where  $r_{\theta}$  and  $p_{\theta}$  are the initial position and momentum, respectively, of the carrier immediately after the last scattering event and

$$\mathbf{r}(t) = \begin{pmatrix} x(t) \\ y(t) \\ z(t) \end{pmatrix} = \begin{pmatrix} x_0 + \frac{p_{0x}}{m^*}t + \frac{q\mathcal{E}_x}{2m^*}t^2 \\ y_0 + \frac{p_{0y}}{m^*}t + \frac{q\mathcal{E}_y}{2m^*}t^2 \\ z_0 + \frac{p_{0z}}{m^*}t + \frac{q\mathcal{E}_z}{2m^*}t^2 \end{pmatrix},$$
(S15)

which, between any two consecutive scattering events, is just a parabola when the applied electric field is constant in magnitude and direction or a straight line in a field with a magnitude of zero. Combining Equation 15 and the equation for the conical boundary yields a quartic equation of the form:

$$c_4 t^4 + c_3 t^3 + c_2 t^2 + c_1 t + c_0 = 0 (S17)$$

for the time solution of the intersection, where

$$c_4 = \left(\frac{q}{2m^*}\right)^2 SDP(\mathcal{E}, \mathcal{E}, a)$$

$$c_3 = \frac{q}{m^{*2}} SDP(\mathbf{p}_0, \mathcal{E}, a)$$
(S18)

$$c_2 = \frac{1}{m^{*2}} SDP(\boldsymbol{p}_0, \boldsymbol{p}_0, a) + \frac{q}{m^*} SDP(\boldsymbol{K}, \boldsymbol{\mathcal{E}}, a)$$

$$c_1 = \frac{2}{m^*} SDP(\boldsymbol{K}, \boldsymbol{p}_0, a)$$

$$c_0 = SDP(\boldsymbol{K}, \boldsymbol{K}, a),$$

where

$$K = r_0 - v. (S19)$$

and SDP is a Special Dot Product function such that

$$SDP(A, B, c) = -c^2 A_x B_x + A_y B_y + A_z B_z,$$
 (S20)

where  $\boldsymbol{A}$  and  $\boldsymbol{B}$  are 3D vectors and  $\boldsymbol{c}$  is a constant.

A typical root finding method can be used here to determine the time solutions of Equation 17.

## **II.** Supporting Figures

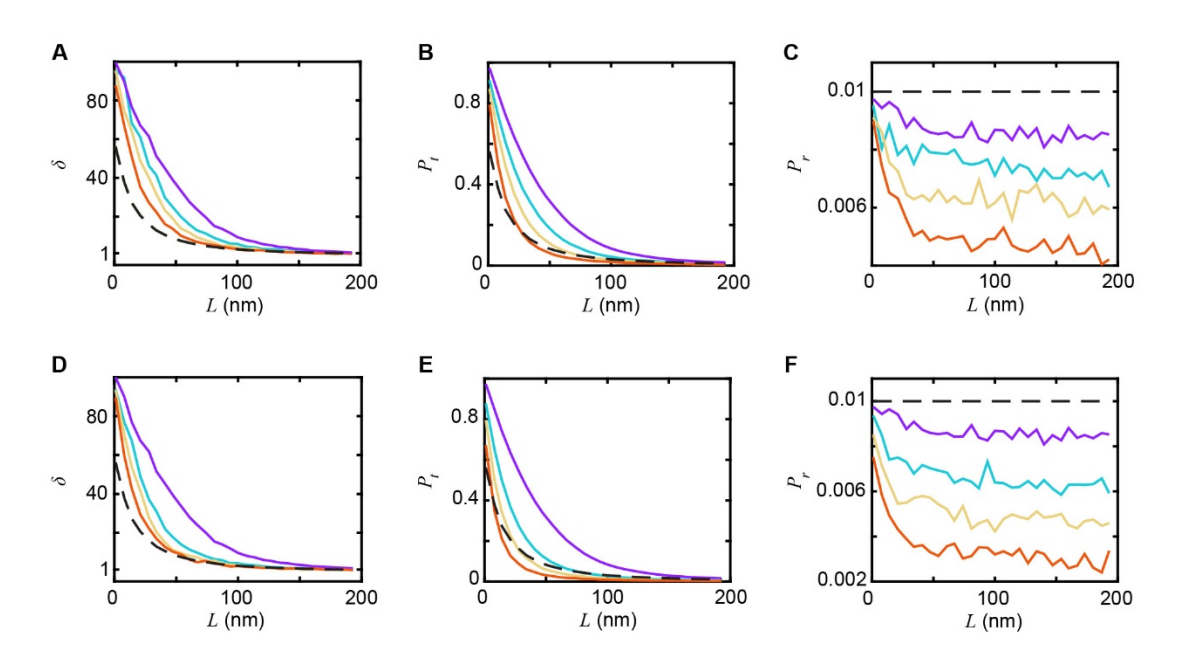
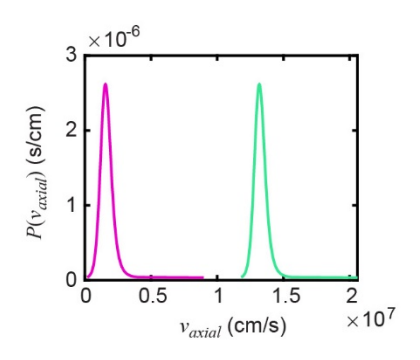


Figure S1. Probabilities of transmission for ballistic simulations with various carrier MFPs.

Plots of (**A**)  $\delta$ , (**B**)  $P_t$ , and (**C**)  $P_r$  at fixed temperature (T = 100 K) and variable  $N_D$  with MFPs of 10 nm (orange), 20 nm (yellow), 35 nm (cyan), and 60 nm (purple) at  $N_D = 10^{17} \text{ cm}^{-3}$ ,  $10^{16} \text{ cm}^{-3}$ ,  $10^{15} \text{ cm}^{-3}$ , and  $10^{13} \text{ cm}^{-3}$ , respectively. Plots of (**D**)  $\delta$ , (**E**)  $P_t$ , and (**F**)  $P_r$  at fixed carrier density ( $N_D = 10^{13} \text{ cm}^{-3}$ ) and variable T with MFPs of 10 nm (orange), 20 nm (yellow), 35 nm (cyan), and 60 nm (purple) at T = 450 K, 300 K, 200 K, and 100 K, respectively. Black dashed lines represent the ratio of the areas of terminal t to terminal t to the constriction (panels B, E), and the ratio of the areas of terminal t to the constriction (panels C, F).



**Figure S2. Initial electron axial velocity.** Probability density,  $P(v_{axial})$ , for the initial charge carrier axial velocity component,  $v_{axial}$ , with (teal) and without (pink) additional kinetic energy imparted by an applied bias.

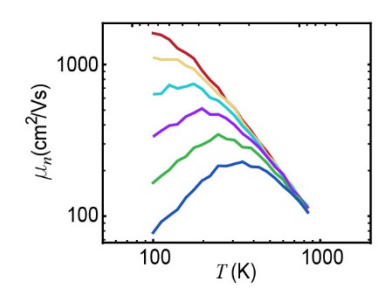


Figure S3. Simulated electron mobility. Plot of electron mobility at T = 100 K to 800 K for  $N_D = 10^{19} \text{ cm}^{-3}$  (blue),  $10^{18} \text{ cm}^{-3}$  (green),  $10^{17} \text{ cm}^{-3}$  (purple),  $10^{16} \text{ cm}^{-3}$  (cyan),  $10^{15} \text{ cm}^{-3}$  (yellow),  $10^{14} \text{ cm}^{-3}$  (red).